Mode identification from time-resolved spectroscopy of the pulsating white dwarf G29-38

J. C. Clemens,[1,2]★ M. H. van Kerkwijk[1,3,4]★ and Y. Wu[5,6]★

[1]*Palomar Observatory, California Institute of Technology 105-24, Pasadena, CA 91125, USA*
[2]*Department of Physics and Astronomy, University of North Carolina, Chapel Hill, NC 27599-3255, USA*
[3]*Institute of Astronomy, University of Cambridge, Madingley Road, Cambridge CB3 0HA*
[4]*Astronomical Institute, Utrecht University, PO Box 80000, 3508 TA Utrecht, the Netherlands*
[5]*Theoretical Astrophysics, California Institute of Technology 130-33, Pasadena, CA 91125, USA*
[6]*Astronomy Unit, School of Mathematical Sciences, Queen Mary and Westfield College, Mile End Road, London E1 4NS*

ABSTRACT

We have used time-resolved spectroscopy to measure the colour dependence of pulsation amplitudes in the DAV white dwarf G29-38. Model atmospheres predict that mode amplitudes should change with wavelength in a manner that depends on the spherical harmonic degree ℓ of the mode. This dependence arises from the convolution of mode geometry with wavelength-dependent limb darkening. Our analysis of the six largest normal modes detected in Keck observations of G29-38 reveals one mode with a colour dependence different from the other five, permitting us to identify the ℓ-value of all six modes and to test the model predictions. The Keck observations also show pulsation amplitudes that are unexpectedly asymmetric within absorption lines. We show that these asymmetries arise from surface motions associated with the non-radial pulsations (which are discussed in detail in a companion paper). By incorporating surface velocity fields into line profile calculations, we are able to produce models that more closely resemble the observations.

Key words: stars: individual: G29-38 – stars: oscillations – white dwarfs.

1 INTRODUCTION

Despite observations over a broad range of wavelengths and via numerous techniques, the star G29-38 remains an enigma. It is the third brightest ZZ Ceti known ($V = 13.05$), and has pulsation amplitudes among the largest measured for these variables (up to 6 per cent modulations at optical wavelengths). It is the most extensively observed large-amplitude ZZ Ceti star, having been the subject of two global observing campaigns (Winget et al. 1990; Kleinman et al. 1994) and of countless single-site time-series measurements (Kleinman et al. 1998). It has also been the target of several infrared and radial velocity studies following the detection of an infrared excess by Zuckerman & Becklin (1987). Nevertheless, we still have neither an unambiguous asteroseismological solution for the star, nor an explanation for the source of the mysterious dust apparently responsible for its excess emission in the infrared.

Recently, Kleinman (1995; see also Kleinman et al. 1998) analysed all of the optical time-series photometry of this object, and showed that, in spite of the changing character of the pulsation spectrum each season, there is a stable set of recurring modes. This is an important breakthrough for G29-38, and perhaps for all the large-amplitude ZZ Ceti stars, because measuring mode periods is a prerequisite for measuring mass and internal structure using stellar seismology. The only remaining obstacle is to identify the spherical harmonic degree ℓ and radial order n of the modes detected, so that their periods can be compared with those of like eigenmodes in structural models of white dwarf stars.

The pattern identified by Kleinman (1995) is sufficiently rich that he was able to attempt mode identification using the same techniques as have been applied successfully to DOV (Winget et al. 1991) and DBV pulsators (Winget et al. 1994). He searched for the (roughly) equal period spacings and frequency splittings that signify rotationally split non-radial g modes. His attempt was a measured success: he found that the pattern of modes was sensible if interpreted as a sequence of mostly $\ell = 1$ modes. Unfortunately, his analysis could not assure that any individual mode was $\ell = 1$, nor did it allow an unambiguous comparison with structural models (Bradley & Kleinman 1996).

With this in mind, and having available to us the bright portion of a night allocated to very faint sources at the Keck II telescope, we decided to test a method for identifying the degree of pulsation modes using G29-38 as our subject. The method was inspired by

---

★ E-mail: clemens@physics.unc.edu (JCC); M.H.vanKerkwijk@astro.uu.nl (MHvK); Y.Wu@qmw.ac.uk (YW)

the work of Robinson et al. (1995), who used *Hubble Space Telescope* high-speed photometry in the ultraviolet to measure ℓ for modes in the star G117-B15A. Their technique exploited the sensitivity of ZZ Ceti mode amplitudes to the wavelength of the observations. At all wavelengths, the observed amplitudes are diminished by cancellation between surface regions with opposite pulsation phase. In the ultraviolet, stronger limb darkening changes the character of this cancellation, and observed mode amplitudes differ from their optical values in a manner that depends on ℓ. The models calculated by Robinson et al. (1995) to explore differences between the ultraviolet and the optical also show amplitude changes within optical absorption lines. The character of these changes likewise depends upon ℓ, providing the potential to determine ℓ from optical spectroscopy.

In an attempt to measure the line profile variations of G29-38 and use them for ℓ identification, we acquired over 4 h of time-resolved spectroscopy using the Keck II Low Resolution Imaging Spectrometer (LRIS: Oke et al. 1995). We have described these observations in a companion paper (van Kerkwijk et al. 2000, hereafter Paper I), and presented an analysis of the periodicities present in the total flux and line-of-sight velocity curves. Prior to our Keck observations, the velocity variations associated with ZZ Ceti pulsations had never been detected. Their presence significantly complicates the models required to understand our data fully, but also increases the amount of valuable information that we can hope to extract.

In this paper we present our analysis of the line profile variations of G29-38. We begin in Section 2, with an analysis of the average spectrum, which has a signal-to-noise ratio higher than usual for white dwarf spectra. In Section 3 we present the amplitudes and phases as a function of wavelength for the largest modes, and compare them with each other and with theoretical models like those calculated by Robinson et al. (1995). On this basis alone it will be clear that we can unambiguously identify ℓ for these modes. It will also be clear that good quantitative fits to the data will require improvements to model atmospheres. None the less, we will continue in Section 4 by incorporating the velocity field associated with the pulsations into the models. The improved models help to constrain other pulsation properties, such as the velocity amplitude of motions at the stellar surface. We present our conclusions in Section 5.

2 THE MEAN SPECTRUM

By averaging together all of our time-series spectra, we have constructed a mean spectrum with extremely high signal-to-noise ratio. This spectrum shows Balmer lines (Hβ to Hι), the Ca II $\lambda 3933$ resonance line, and a hint of Mg II $\lambda 4481$ (Paper I). Metal lines were first discovered in G29-38 by Koester, Provencal & Shipman (1997), who also found iron lines in the ultraviolet spectrum. The presence of metals in a DA spectrum is unusual, and Koester et al. (1997) attribute them to the accretion of dust, supporting the notion that the infrared excess in the spectrum of G29-38 is caused by reprocessing of light by circumstellar dust grains.

We have fitted the Balmer lines in our mean spectrum using a grid of model spectra kindly provided by D. Koester (for a recent description, see Finley, Koester & Basri 1997). The models consist of tabulated intensities, I_λ, at nine limb angles, $\mu = \cos\theta$, for a grid of atmospheres with effective temperatures spanning the ZZ Ceti instability strip and with gravities from $\log g = 7.50$ to 8.75.

The atmospheres were all calculated using the ML2, $\alpha = 0.6$ prescription for convection, which yields consistent fits for ZZ Ceti stars over the broadest range of wavelengths (Bergeron et al. 1995). To compare the models with our spectrum we integrated I_λ over the visible hemisphere and compared the resulting Balmer lines with those that we observed by normalizing both model and data to fixed continuum points. This method is similar to that used by Bergeron, Saffer & Liebert (1992), but less sophisticated than the procedure that Bergeron et al. (1995) used for their analysis of ZZ Ceti spectra.

Fig. 1 shows the observed Balmer lines along with the best-fitting model, which has $T_{\mathrm{eff}} = 11\,850$ K and $\log g = 8.05$. These values are close to those published for G29-38 by Bergeron et al. (1995) and Koester et al. (1997). The former found $T_{\mathrm{eff}} = 11\,820$ K and $\log g = 8.14$, the latter $T_{\mathrm{eff}} = 11\,600$ K and $\log g = 8.05$. Using the evolutionary models of Wood (1994) with thick surface H layers ($\sim 10^{-4} M_*$), our values translate into a mass of $0.64\,M_\odot$.

As impressive as the fit in Fig. 1 is, the discrepancies between model and data are still dominated by systematic effects, rather than stochastic noise. This makes the values of χ^2 that we calculate useless for evaluating the error in our temperature and gravity determination; the error is dominated by real differences between the models and the measurements. These differences might arise from a variety of sources.

One possibility is that the normalization of our data to the continuum points was affected by errors in our calibration of the instrumental response. Another possibility is that errors arise from the presence of metal lines not included in the models. The shapes of H8 = Hζ and Hϵ are probably affected by depression of the intervening continuum by the Ca II $\lambda 3933$ line, and Hϵ is contaminated by Ca II $\lambda 3968$. However, the metal lines cannot entirely account for the problem, because the fits to Hβ, Hγ and Hδ, which should be unaffected by metals, are also less than perfect.

The discrepancy in the fits might also be due to a problem discussed by Koester, Allard & Vauclair (1994). They found that even the best prescription for convection yields a temperature structure in model atmospheres that is only approximately correct. Consequently, the synthetic spectra that the models produce will not match observed spectra at every wavelength simultaneously,
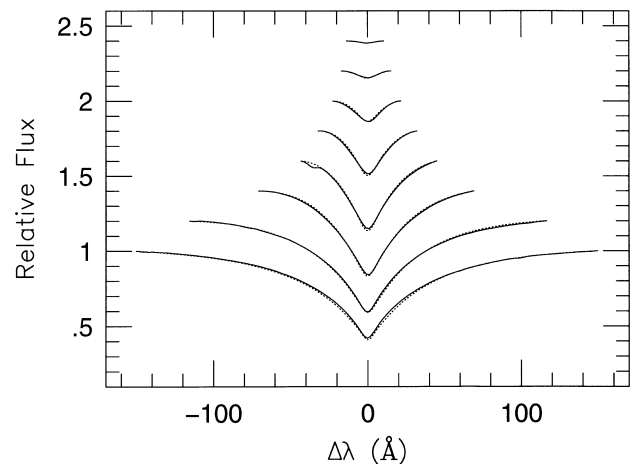

Figure 1. The best overall fit to the line profiles Hβ to H11 in the average spectrum of G29-38. The model (dotted line) has $\log g = 8.05$ and $T_{\mathrm{eff}} = 11\,850$ K. The dip on the blue side of Hϵ is the Ca II $\lambda 3933$ line.
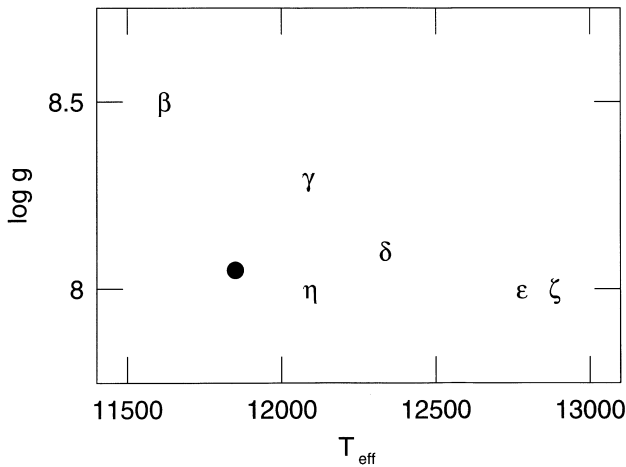
Figure 2. Location of best fits to the individual Balmer lines in the T_{eff} − $\log g$ plane. Fits to individual lines are denoted by the line designations; the best fit using all the lines (see Fig. 1) is shown as a filled circle.

nor will they match all the line profiles, which are highly sensitive to the run of temperature with depth. To explore this possibility, and to see how our final fit is affected by individual lines, we have fitted separate models to each of the Balmer lines.

In Fig. 2, we plot the values of $\log g$ and T_{eff} for the best-fitting models of the individual lines Hβ to H9. They span a range of temperature from 11 620 to 12 885 K. With the exception of H9 = Hη, the fits show a trend to higher T_{eff} and lower $\log g$ as the excitation level increases. The location of the fit using all lines compared with the individual lines shows that the gravity fit is dominated by the lines of higher excitation, which are known to be more gravity-sensitive. Conversely, the temperature is fixed by the lower excitation lines, which change more rapidly with T_{eff}.

Fig. 2 is not meant to suggest that the individual fits give answers inconsistent with the global fit; rather, they should be regarded as helping to establish the uncertainty of the temperature and gravity determination. It is clear that high signal-to-noise ratio alone is not enough to improve the determination of temperature and gravity. Better calibration of the instrument or improvements to the models (or both) will be necessary. The systematic trend in the individual Balmer line fits suggests that the problem lies with the models, as do the results of the following section. There we compare fractional amplitudes calculated from data and models, and find further discrepancies. In the fractional amplitudes, calibration errors should cancel to first order.

If the models turn out to be responsible for the discrepancies that we measure, our high signal-to-noise ratio average spectrum will provide the opportunity to improve atmospheric models, perhaps even to infer the correct temperature profile. Furthermore, individual spectra in our time series, which themselves have a signal-to-noise ratio of 100, span a temperature range of about 500 K and will show how the atmospheric structure should change with model temperature. This information about the derivative of the thermal profile should provide extremely valuable constraints on model atmospheres. Our data are available upon request to anyone interested in exploring these problems.

The final factor that might affect our model fit is the presence of relatively large-amplitude pulsations. We have shown in Paper I that the velocity fields associated with the pulsations of G29-38 are detectable in our data. These motions alter the average spectrum, mainly by Doppler broadening the absorption lines very
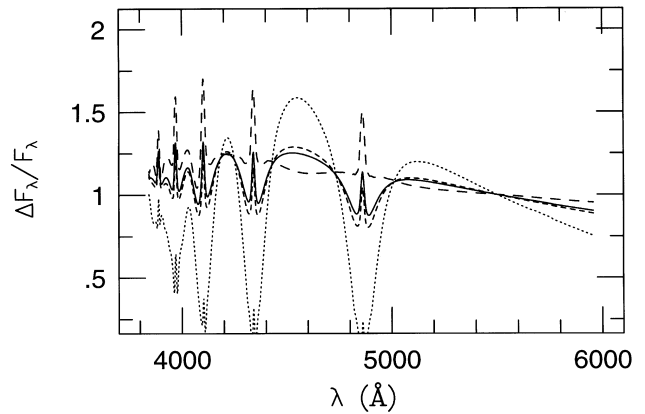

Figure 3. Models for the wavelength-dependent flux variations for modes of ℓ = 1–4, after Robinson et al. (1995). We have used the values of $\log g$ and T_{eff} from our best fit to the average spectrum and convolved the output with a Gaussian of 5-Å width to match our Keck observations. All curves are normalized at 5500 Å. The solid line is for ℓ = 1, the short-dashed line is for ℓ = 2, the dotted line is for ℓ = 3, and the long-dashed line is for ℓ = 4.

slightly. The models that we will describe in Section 4 allow us to incorporate this effect into the model spectrum. Fitting the data with these velocity-broadened spectra yields a slight improvement in the quality of the fit to the average spectrum, but an insubstantial change in the values of $\log g$ and T_{eff} that we infer from the models.

3 LINE PROFILE VARIATIONS

Robinson et al. (1995) have described and implemented a method for distinguishing the value of ℓ in ZZ Ceti stars by comparing pulsation amplitudes at different wavelengths. Their method relies upon the increased importance of limb darkening in the ultraviolet. Non-radial pulsation modes of every ℓ suffer from geometric dilution in their amplitudes when averaged over the visible hemisphere. This dilution increases with ℓ as cancellation between regions with opposing phase becomes important. However, at short wavelengths increased limb darkening diminishes the effect of the cancellations. For $\ell \leqslant 3$, the net result is that mode amplitudes increase in the ultraviolet relative to their optical values in a way that depends on ℓ. Robinson et al. (1995) used optical and ultraviolet high-speed photometry to measure this effect for the 215-s pulsation mode in G117-B15A. They were able to conclude that this mode is ℓ = 1. Fontaine et al. (1997) re-analysed the same data using independent models and arrived at the same conclusion, although they differed from Robinson et al. in the model temperature that best fits the data.

The models that Robinson et al. (1995) calculated also showed ℓ-dependent differences in the behaviour of pulsation amplitudes within the absorption lines. These too arise from the effects of limb darkening on modes of different ℓ. Fig. 3 shows these changes for low values of ℓ, which are expected to dominate the modes observed in white dwarfs. We calculated these curves using a modified version of code originally provided to us by E. L. Robinson (see Robinson et al. 1995). Instead of integrating over a limb-darkening law, we integrate over intensities tabulated for different values of μ, as described in Section 2. Consequently, equations (3a) and (3b) in Robinson et al., which represent the equilibrium flux and the flux changes arising from the pulsations,

become

$$F_\lambda = 2\pi R_0^2 \int_0^1 I_\lambda(g, T_0, \mu)\mu\, d\mu \qquad (1)$$

and

$$\Delta F_\lambda = 2\pi R_0^2 \left(R_0 \frac{\delta T}{\delta R} \right) \epsilon k_{\ell m} \cos(\sigma t)$$
$$\times \int_0^1 \frac{\partial I_\lambda(g, T, \mu)}{\partial T}\bigg|_{T_0} P_\ell(\mu)\mu\, d\mu. \qquad (2)$$

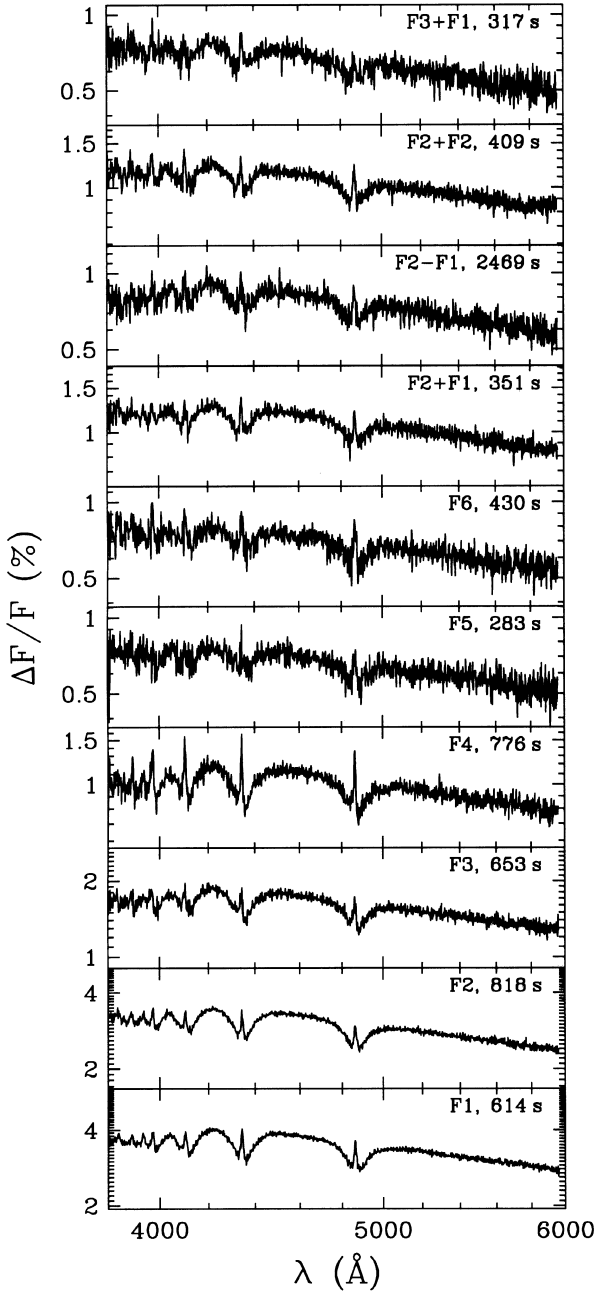Here, R_0 is the equilibrium stellar radius, T_0 is the equilibrium

Figure 4. Wavelength-dependent amplitudes for the six largest modes and four largest combination frequencies in G29-38. To ease comparison, the same logarithmic scale was used for all panels. Note the small peak seen in the amplitudes of F1 at 3933 Å, corresponding to the Ca II line.

temperature, ϵ is the amplitude of the radius changes induced by the pulsations, and $\delta T/\delta R$ is the Lagrangian derivative of temperature with respect to radius. Together $P_\ell(\mu)$ and $k_{\ell m}$ represent the surface distribution of the temperature changes after integrating in the ϕ-direction. $P_\ell(\mu)$ is a Legendre polynomial depending only on μ, and $k_{\ell m}$ depends on the angle between the pulsation axis and the observer's line of sight. Our notation is slightly different from Robinson et al. (1995) in that we have separated the time dependence, $\cos(\sigma t)$, from $k_{\ell m}$. Finally, while $I_\lambda(g, T, \mu)$ comes directly from the tabulated models, $\partial I_\lambda(g, T, \mu)/\partial T$ must be calculated by taking differences between models of different T_{eff}.

Robinson et al. (1995) have emphasized the useful properties of the ratio $\Delta F_\lambda/F_\lambda$ for ℓ identification. It is not sensitive to the flux calibration of the data and varies with wavelength in a way that does not depend on mode inclination and m (see also the Appendix). In Fig. 3 we show $\Delta F_\lambda/F_\lambda$ for modes of $\ell = 1$–4. The curves have been normalized to 1 at 5500 Å. We have not included $\ell = 0$, which resembles $\ell = 1$ with slightly smaller modulations, because it is clear from the long periods of the modes that they cannot be radial pulsations.

In order to compare our data with the models in Fig. 3, we have fitted the amplitudes and phases of the 11 largest pulsation frequencies in each 2-Å wavelength bin using the function $A\cos(2\pi ft - \phi)$. During these fits, we held the mode frequency, f, constant at the values tabulated in Paper I, and fitted the 11 amplitudes and phases simultaneously. Of these 11 modes, five are combination frequencies, i.e. frequencies that have values that are sums or differences of larger modes. We have discussed the nature of combination frequencies in Paper I and will return to them at the end of this section. Fig. 4 shows the fractional amplitudes at each wavelength for the six physical modes and for the four largest combination frequencies. The fifth, F3−F1 at 10 322 s, we judged too noisy to include. The qualitative similarity between the data and the models is striking. Even in the line cores the models predict the behaviour of mode amplitudes quite well, despite the fact that, within ~1 Å of the core, non-LTE effects in the atmosphere (which are difficult to model) are important. We emphasize that these are predictions in the literal sense: Koester calculated the atmospheric models before we acquired the data.

In the models that we have discussed so far, the pulsations have the same phase at every wavelength. However, the phases of the physical modes, shown in Fig. 5, show distinct changes in the vicinity of spectral features. For mode F1, the phase changes within absorption lines bear the signature of a velocity-induced variation; they change with the derivative of the spectrum. We will return to these phase changes in Section 4, when we have models capable of reproducing them. In addition to the phase changes within the lines, Fig. 5 also shows a small slope in the continuum phases, indicating that pulse maximum in blue light arrives earlier than in red by a few seconds. This slope is not reproduced by our models, and remains a mystery.

Careful inspection of the amplitudes of the real modes in Fig. 4 reveals that those for mode F4, at 776 s, show a different shape from those for the other modes: they increase more sharply in the line cores and curve more steeply in the continuum. F4 was already noticeably different from the other real modes in Paper I, where we found that it had a larger velocity-to-light amplitude ratio than any of the other modes, and it produced a stronger harmonic.

To help see the differences in F4, we have normalized the amplitudes of F1 and F4 at 5500 Å and plotted the modes together
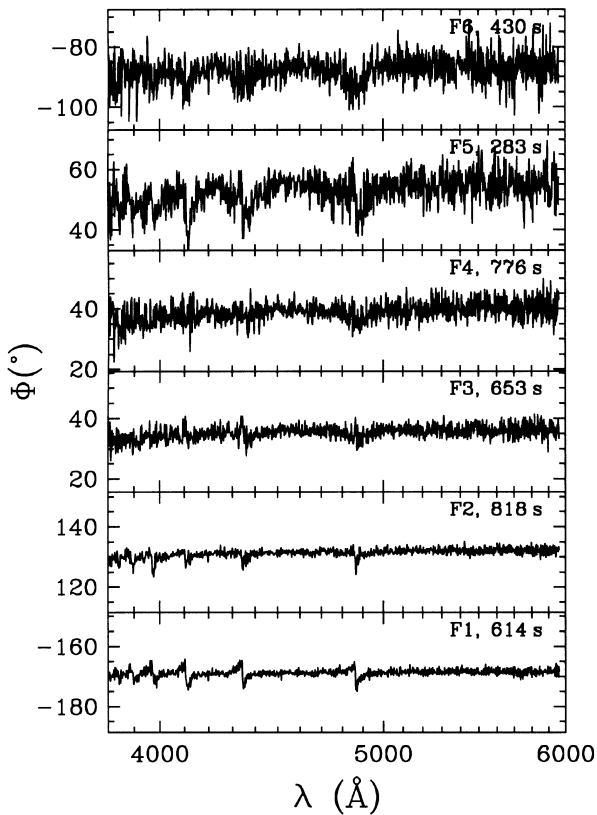
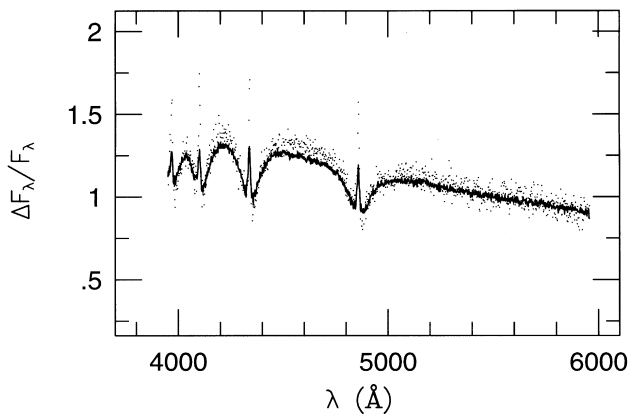**Figure 5.** Wavelength-dependent phases for the six largest normal modes in G29-38.

Figure 6. Amplitude comparison for F1 (solid line) and F4 (discrete points). The amplitudes have been normalized to 1 at 5500 Å.

Figure 7. Comparison with models for modes 1, 2, 4 and 5. The solid line is for $\ell = 1$; the dashed line is for $\ell = 2$. The models were calculated using $\log g = 8.05$ and equilibrium $T_{\text{eff}} = 11\,850\,\text{K}$, as derived from the fits to the average spectrum.

in Fig. 6. The most likely explanation for the differences that we see is that F4 has a value of ℓ different from F1. Qualitative application of the theoretical models demands that ℓ must be higher for F4, to yield the larger changes in amplitude that we observe. Furthermore, the large contrast between modes of $\ell = 2$ and higher in the models, versus the more modest differences seen in Fig. 6, points toward the conclusion that F4 is $\ell = 2$ and F1 is $\ell = 1$.

To test this possibility further, we can make a direct comparison between the data and models. In Fig. 7 we have plotted the theoretical and observed amplitudes for modes 1, 2, 4 and 5. To establish the normalization, we multiplied the theoretical curves
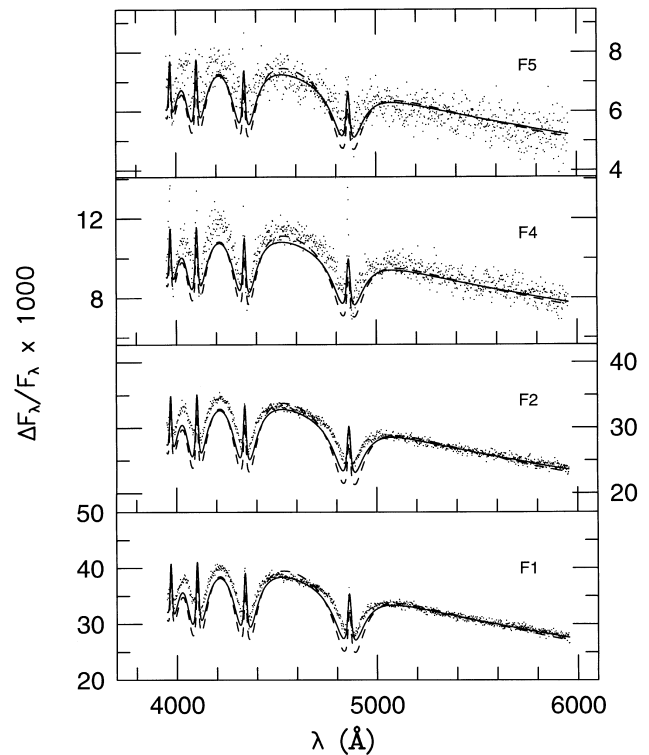
by the amplitudes of each mode at 5500 Å. We have used a model with gravity and equilibrium temperature inferred from our fit to the average spectrum in Section 2. As with the average spectrum, Fig. 7 shows discrepancies between the data and the models. The slope of the amplitude changes is steeper in the data than in the models, worsening the fit at short wavelengths. Correcting this would require hotter models at shorter wavelengths, the same trend as is required to fit to individual Balmer lines in the average spectrum. We could not find a model at any single temperature that offered a substantially better fit than the model we have used.

In spite of the difficulties with the fits, it is clear that $\ell = 1$ is a better match to modes F1, F2 and F5, while $\ell = 2$ is a better fit to mode F4. Interestingly, this is most apparent in the continuum variations between 4500 and 4700 Å; the models are too poor a fit within the lines to provide a measure of ℓ there. None the less, our original expectation that the line profiles would offer the most sensitive ℓ discriminant are borne out by the large differences between the amplitudes at line centre in F4 and those in the other modes. We have included F5 as the representative of the noisier low-amplitude modes. Even with the higher noise it is clear that $\ell = 1$ is a better fit to this mode, as it is to every mode except mode F4.

Even though the quantitative agreement is poor at many wavelengths, the presence of two apparently different values of ℓ makes our identification secure. The values of ℓ chosen are independent of the model temperature. Lowering the effective temperature of the model chosen diminishes the changes in mode amplitudes, so that, at some T, the $\ell = 2$ model would fit mode F1 and those like it, but at that temperature no value of ℓ fits F4. Likewise, attempts to fit F4 with $\ell = 1$ by increasing model
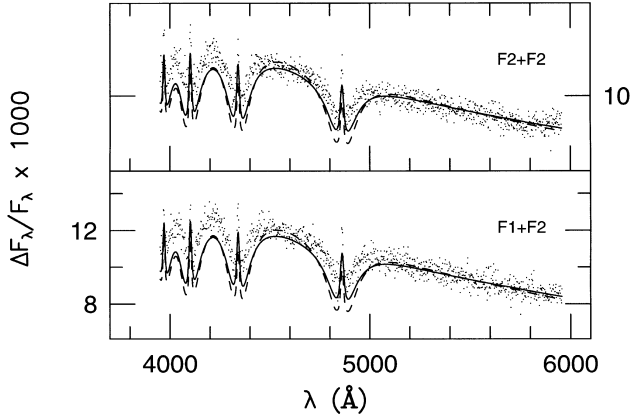
Figure 8. Comparison with models for frequencies F1+F2 and F2+F2. The solid line is for $\ell = 1$; the dashed line is for $\ell = 2$.

temperature leave no ℓ of lower value to fit the other modes. Consequently, on the basis of qualitative behaviour alone, we can conclude that the 776-s mode is $\ell = 2$, and the remaining five modes are $\ell = 1$.

Finally, we consider the combination modes shown in Fig. 4. The combination frequencies that we see in G29-38 and other ZZ Ceti stars probably arise not from eigenmode pulsations, but from a non-linear transformation of the modes in the outer layers of the white dwarf (Brickhill 1992; cf. Brassard, Fontaine & Wesemael 1995). This mixes the modes present, generating signals at sums and differences of the mode frequencies. The ℓ character of these modes depends on the ℓ of the modes that produce them. For example, we expect the combination of two $(\ell, m) = (1, 0)$ modes to have $\ell = 0$ and 2 components, while those of two $(1, -1)$ modes or two $(1,1)$ modes should produce only $\ell = 2$. These expectations arise from the mathematical properties of spherical harmonics only. It is impossible to make quantitative predictions about combination modes without a detailed theory explaining how they are produced. We have shown two combination frequencies along with models in Fig. 8. Like the other combinations, they most resemble the modes that we have identified as $\ell = 1$.

4 MODELS INCLUDING VELOCITIES

Apart from the problems with quantitative fits to the model atmospheres, there is a significant qualitative difference between the observed and model amplitudes in Fig. 7: the observed amplitudes are asymmetric within the absorption lines, while the model amplitudes are not. We showed in Paper I that the Balmer lines not only show changes in flux during a pulsation cycle, but also show changes in line-of-sight velocity. In that paper, we treated these as separable components of the spectral variations, but in reality they are components of a more complex line profile variation. In anticipation of improvements in the model fits, in this section we will calculate these variations by incorporating velocities into the flux integrals that we calculate at each wavelength. This requires that we follow a more general treatment than that used by Robinson et al. (1995) to produce equation (1). Our development will rely upon Robinson, Kepler & Nather (1982) and use the same notation where possible.

The effect of the velocity field on our calculations of the integrated flux is that the values of I_λ that we look up from the tabulated spectra, and the values of $\partial I_\lambda / \partial T$ that we calculate from

them, must be chosen using wavelengths adjusted for the velocity of each surface element. Thus I_λ in equation (1) and $\partial I_\lambda / \partial T$ in equation (2) are now functions of velocity. Since the velocity has a time dependence, both quantities are now also implicit functions of time. We may write the total flux at each observed wavelength as a function of time as

$$F(\lambda_{\rm obs}, t) = F_{T_0}(\lambda_{\rm obs}) + \Delta F_T(\lambda_{\rm obs}, t), \tag{3}$$

where the T_0 is a reminder that the first term comes from the model at equilibrium temperature, and the T indicates that the flux changes in the second term are due to changes in temperature, which dominate all other sources (Robinson et al. 1982). It will help in understanding equation (3) to think about two different limits. The first is a (hypothetical) pulsation mode which has surface motions but no temperature changes. For these modes, the second term would be 0. The first term would be a function of time for any $\lambda_{\rm obs}$ near spectral features that could be Doppler shifted in and out of $\lambda_{\rm obs}$ by the changing velocities. The second limit to think of is a mode with temperature but no velocity variations; then the two terms in equation (3) reduce to the expressions given by equations (1) and (2). An important feature of equation (3) that is not present in equations (1) and (2) is the possibility for the phase of flux maximum to differ from the phase of temperature maximum. This means that the time of flux maximum can differ with wavelength, a possibility that was never allowed by equation (1).

Our expressions for the terms in equation (3) must also be more general than before. We can write F_{T_0} generally as

$$F_{T_0}(\lambda_{\rm obs}) = R_0^2 \int_0^{2\pi} \int_0^1 I(g, T_0, \mu, \lambda) \mu \, d\mu \, d\phi, \tag{4}$$

which is analogous to the expression used by Kepler (1984) in his discussion of line profile variations arising from r-mode pulsations. As we have noted, the time-dependent velocities enter into the wavelength λ, so $F_{T_0}(\lambda_{\rm obs})$ is a function of time. Likewise, ΔF_T is given by

$$\Delta F_T(\lambda_{\rm obs}, t) = \left(R_0 \frac{\delta T}{\delta r} \right) \epsilon R_0^2 \, e^{-i\psi}$$
$$\times \int_0^{2\pi} \int_0^1 \left. \frac{\partial I(g, T, \mu, \lambda)}{\partial T} \right|_{T_0} \xi_r \, \mu \, d\mu \, d\phi, \tag{5}$$

where ξ_r is the assumed functional form for the perturbations in stellar radius,

$$\xi_r = Y_{\ell m}(\Theta, \Phi) e^{i\sigma t}. \tag{6}$$

$Y_{\ell m}(\Theta, \Phi)$ is the spherical harmonic of degree ℓ and order m in the coordinate system (Θ, Φ) aligned with the pulsation axis, and σ is the pulsation frequency. Compared with equation (2), we have reverted to an expression in which the imaginary parts of the temporal and spatial dependences are included; moreover, we have followed Robinson et al. (1982) in adopting an extra term $e^{-i\psi}$ to allow for the non-adiabatic effects which may introduce a phase difference between the radial displacement and the flux changes.[1] The negative sign in the exponent indicates that, for

---

[1] In Robinson et al. (1982), equations (20), (23) and (24) should not have negative signs on their right-hand sides. The quantity $\delta T / \delta r$ is positive for adiabatic pulsations, since maximum radial displacement corresponds to maximum temperature. This has no effect on any of the conclusions that Robinson et al. presented.

positive values of ψ, maximum flux lags maximum radial displacement.

In equations (4) and (5), the value of λ should be the wavelength from which light is Doppler shifted into $\lambda_{\rm obs}$, or

$$\lambda = \lambda_{\rm obs}\left[1 - \frac{v_{\rm rad}(\mu, \phi, t)}{c}\right] \tag{7}$$

to first order. We use $v_{\rm rad}$ to express the velocity component projected into our line of sight. Calculating $v_{\rm rad}$ requires first an expression for the pulsation velocities at the stellar surface.

In the frame of reference (Θ, Φ) aligned with the pulsation axis, the components of the pulsation velocities are, following Dziembowski (1977),

$$V_r = i\sigma\epsilon R_0 Y_{\ell m}(\Theta, \Phi)\, e^{i\sigma t},$$

$$V_\Theta = \frac{i\epsilon|g|}{\sigma}\frac{\partial Y_{\ell m}(\Theta, \Phi)}{\partial \Theta}\, e^{i\sigma t} \text{ and}$$

$$V_\Phi = -\frac{i\epsilon|g|}{\sigma}\frac{m}{\sin\Theta} Y_{\ell m}(\Theta, \Phi)\, e^{i\sigma t}. \tag{8}$$

For g-mode pulsations, V_r is small compared with the other two, and can be ignored.

To get $v_{\rm rad}$ requires transforming the remaining velocity expressions into our reference frame and projecting them along our line of sight. Then equations (3)–(7) are all that we need in principle to calculate colour-dependent pulsation amplitudes in the presence of non-zero velocities. In practice, this would be cumbersome and inefficient for arbitrary inclination and m, so we have further simplified the problem by aligning the pulsation axis with our line of sight and holding $m = 0$. Contrary to initial expectations, this simplification comes at almost no expense; the results for this case scale easily to arbitrary choices for inclination and m. In the Appendix we demonstrate that this is true and show how the scaling is done.

This simplification allows us to dispense with the expression for V_Φ and to replace Θ and Φ in all equations with θ and ϕ for our reference frame. The ϕ dependences of $v_{\rm rad}$, ξ_r and I_λ also disappear, and the spherical harmonics reduce to Legendre polynomials. Finally, to make our fits independent of the particular choices for stellar radius and pulsation frequency, we have introduced the fitting parameters

$$a_T = R_0\left|\frac{\delta T}{\delta r}\right|\epsilon \text{ and}$$

$$a_v = \frac{\epsilon g}{\sigma}. \tag{9}$$

Thus the final expressions that we evaluate numerically are

$$F_{T_0}(\lambda_{\rm obs}) = 2\pi R_0^2\int_0^1 I\left[g, T_0, \mu, \lambda_{\rm obs}\left(1 - \frac{v_{\rm rad}}{c}\right)\right]\mu\, d\mu,$$

$$\Delta F_T(\lambda_{\rm obs}, t) = 2\pi R_0^2 a_T \cos(\sigma t - \psi)$$

$$\times \int_0^1 \left.\frac{\partial I\left[g, T, \mu, \lambda_{\rm obs}\left(1 - \frac{v_{\rm rad}}{c}\right)\right]}{\partial T}\right|_{T_0} P_\ell(\mu)\mu\, d\mu,$$

$$v_{\rm rad}(\mu, t) = -a_v\frac{dP_\ell(\mu)}{d\theta}\sin\theta\sin(\sigma t), \tag{10}$$

where we have kept only the real parts of the temporal variations. The free parameters in these equations are the temperature and gravity of the equilibrium model, T_0 and g, the (non-adiabatic)

phase shift ψ, and the amplitudes given by equation (9). The equilibrium radius, R_0, cancels when we calculate the fractional amplitude.

We have modified the code originally provided by E. L. Robinson to perform these integrals at a series of time-steps covering one pulsation cycle. Then we have convolved the output spectra with a Gaussian to emulate seeing. Finally, we have calculated the pulsation amplitude, phase and mean spectrum at each wavelength.

In Paper I, we defined the quantity $\Delta\Phi_V$ as the phase difference between maximum light and maximum velocity. In the formalism of this paper,

$$\Delta\Phi_V = \frac{\pi}{2} - \psi. \tag{11}$$

For the $\psi = 0$ case, where flux and radial displacement are in phase, the $\pi/2$ delay enters because of the time derivative used to get $v_{\rm rad}$. Positive values of ψ then reduce $\Delta\Phi_V$ by delaying the maximum light so that it arrives less than $\pi/2$ before maximum velocity. In all of the modes for which we can detect velocities, $\Delta\Phi_V$ lies in the first quadrant, implying that flux maximum is delayed compared with the adiabatic case (or velocity maximum advanced, which is harder to imagine). This is a profound result, and the first direct observational constraint on the behaviour of eigenmodes near the surface of a white dwarf star.

Comparing our models with the data presents something of a challenge, because of the generally poor match for any choice of amplitude and phase. We have simplified the problem by choosing the equilibrium temperature and gravity from our fit to the average spectrum. Then we have fitted a_T directly, by insisting that the fractional amplitude of the flux changes in our model matches those in the data at 5500 Å. To choose appropriate values for a_v and ψ, we used our model to calculate several time series of synthetic spectra, and then we reduced them in the same way as the real data. This allowed us to calibrate the scaling introduced by the integrals in equation (10) for various choices of ℓ, a_v and ψ. Then we used these scale factors to generate models based on the properties measured for modes in Paper I. The size of the velocities that we use to match our data is quite similar to the size predicted by Robinson et al. (1982), $\sim 7\,{\rm km\,s^{-1}}$.

Fig. 9 shows the results of these calculations for the Hβ line in modes F1 and F4. Our models now reproduce the asymmetry in the amplitude plots, and show phase changes within the line profiles. These phase changes could never be reproduced without including velocities in the models. However, the overall quality of the amplitude fits within lines is not much improved, and is not changed at all in the continuum. The phases are a good fit within spectral lines for the larger modes, but our models still do not reproduce the slow change in phase observed in the continuum (see Fig. 5). For now, this remains a mystery, but probably a mystery hiding interesting pulsation physics.

Finally, we consider the behaviour of the ratio between the observed velocity and flux amplitudes. As we show in the Appendix, this ratio does not depend on the inclination or m of the modes, and therefore cannot be used to constrain those quantities. However, it is sensitive to the value of ℓ, as evident from the different forms for flux and velocity in the integrals of equation (10). The flux depends on the Legendre polynomial, while the velocity depends on its derivative and in addition is weighted towards the limb by the projection on to the line of sight. According to our models, for a fixed value of a_v/a_T, an $\ell = 2$ mode should have a factor of ~ 4 higher apparent velocity-to-light
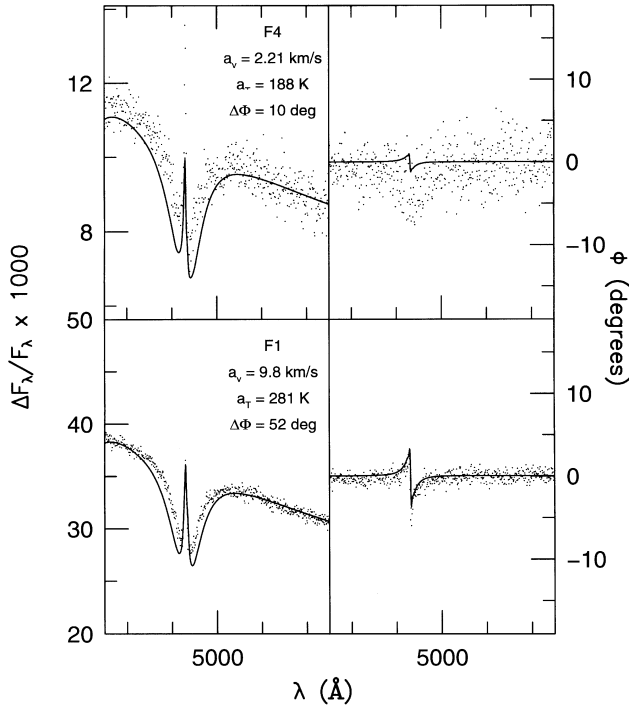
Figure 9. Fits to F1 and F4 including velocities. The amplitudes listed are those described by equation (9) in the text.

ratio than an $\ell = 1$ mode. It is then no surprise that mode F4, which we have identified as $\ell = 2$, has the highest velocity-to-light amplitude ratio (see Paper I) of any of the modes that we have detected, a result which supports our identification of that mode as $\ell = 2$.

5   SUMMARY AND CONCLUSIONS

Asteroseismology of ZZ Ceti stars has been impeded for almost two decades by the lack of a reliable method for mode identification. We have tested a new method that uses high signal-to-noise ratio time-resolved spectroscopy to measure the wavelength dependence of optical pulsation amplitudes. We have found that the ℓ-dependent changes in amplitude predicted by the models are also present in our data, allowing us to assign values of ℓ to six modes in the star G29-38.

Initially, this will be of greatest benefit to seismological models of G29-38. None of the modes that we have identified is short enough to yield immediate constraints on the mass of the H layer, as is possible for G117-B15A (Robinson et al. 1995), GD 165 (Bergeron et al. 1993) and G226-29 (Fontaine et al. 1992). However, a concerted effort to match the six modes of known ℓ may yield a unique solution. If not, it is possible to return to this star with the hope that four more hours of data will allow identification of a different set of modes. Sooner or later, we will have a definitive asteroseismological solution for this star; the main obstacle has been removed.

Our method can also be extended to other ZZ Ceti stars, although the fainter, low-amplitude stars will require longer runs. We have already begun a programme to identify ℓ in as many stars as is practical in the observing time available to us. This programme should allow us to measure structural properties of enough stars to answer some long-standing questions about the DA stars, such as the masses of the H and He surface layers, which

have been the subject of some controversy (Shipman 1996; Fontaine & Wesemael 1996).

Apart from the impact that our results will have on ZZ Ceti seismology, they have also opened new windows into the surface physics of pulsating white dwarfs. We have measured two new diagnostics of the behaviour of pulsations near the photosphere: the amplitude of the pulsation velocities, and the phase lag between flux maximum and velocity maximum. These can be compared quantitatively with predictions of non-adiabatic pulsation theories (e.g. Lee & Bradley 1993; Wu & Goldreich 1999), as well as with measurements for other stars. We have already detected velocity changes in one other star (HL Tau 76).

Finally, our high signal-to-noise ratio measurements provide a serious challenge to the atmospheric model fits. There are significant discrepancies between the models and our average spectrum, and between the models and the spectral changes caused by pulsation. We have not identified the source of these differences, but hopefully our data and future data like them will provide assistance to modellers in their continuing attempts to understand the atmospheres of white dwarf stars.

REFERENCES

Bergeron P., Saffer R. A., Liebert J., 1992, ApJ, 394, 228
Bergeron P. et al., 1993, AJ, 106, 1987
Bergeron P., Wesemael F., Lamontagne R., Fontaine G., Saffer R. A., Allard N. F., 1995, ApJ, 449, 258
Bradley P., Kleinman S., 1996, in Isern J., Hernanz M., Garcia-Berro E., eds, White Dwarfs. Kluwer, Dordrecht, p. 445
Brassard P., Fontaine G., Wesemael F., 1995, ApJS, 96, 545
Brickhill A. J., 1992, MNRAS, 259, 529
Dziembowski W., 1997, Acta Astron., 27, 203
Finley D. S., Koester D., Basri G., 1997, ApJ, 488, 375
Fontaine G., Wesemael F., 1996, in Isern J., Hernanz M., Garcia-Berro E., eds, White Dwarfs. Kluwer, Dordrecht, p. 173
Fontaine G., Brassard P., Bergeron P., Wesemael F., 1992, ApJ, 399, L91
Fontaine G., Brassard P., Bergeron P., Wesemael F., 1997, ApJ, 469, 320
Kepler S. O., 1984, ApJ, 286, 314
Kleinman S. J., 1995, PhD thesis, University of Texas at Austin
Kleinman S. J. et al., 1994, ApJ, 436, 875
Kleinman S. J. et al., 1998, ApJ, 495, 424
Koester D., Allard N. F., Vauclair G., 1994, A&A, 291, L9
Koester D., Provencal J., Shipman H. L., 1997, A&A, 230, L57
Lee U., Bradley P. A., 1993, ApJ, 418, 855
Oke J. B. et al., 1995, PASP, 107, 375

Robinson E. L., Kepler S. O., Nather R. E., 1982, ApJ, 259, 219
Robinson E. L. et al., 1995, ApJ, 438, 908
Shipman H. L., 1996, in Isern J., Hernanz M., Garcia-Berro E., eds, White Dwarfs. Kluwer, Dordrecht, p. 165
Van Kerkwijk M. H., Clemens J. C., Wu Y., 2000, MNRAS, 314, 209 (Paper I, this issue)
Winget D. E. et al., 1990, ApJ, 357, 630
Winget D. E. et al., 1991, ApJ, 378, 326
Winget D. E. et al., 1994, ApJ, 430, 839
Wood M. A., 1994, BAAS, 185, 4601
Wu Y., Goldreich P., 1999, ApJ, 519, 783
Zuckerman B., Becklin E. E., 1987, Nat, 330, 138

APPENDIX A: ARBITRARY INCLINATION AND VALUE OF m

The usual way to transform an arbitrary spherical harmonic into the coordinate system aligned with our line of sight is to recognize that the $2\ell + 1$ spherical harmonics of a given ℓ form a complete basis set, so it is always possible to express an arbitrary spherical harmonic as a sum of spherical harmonics in our coordinate system,

$$Y_{\ell m}(\Theta, \Phi) = \sum_{m'=-\ell}^{\ell} R^{\ell}_{m'm} Y_{\ell m'}(\theta, \phi). \qquad (A1)$$

The coefficients $R^{\ell}_{m'm}$ are a function of the inclination angle (see Dziembowski 1977; Robinson et al. 1982). Then the $m' \neq 0$ terms of the sum cancel to zero in any integration over the visible hemisphere, so that only the $m' = 0$ term aligned with our line of sight remains.

This will not work directly for the expressions that we integrate in equations (4) and (5), because they contain $I(g, T, \mu, \lambda)$ and its derivative with respect to T, which may be arbitrarily complex functions of the eigenmode velocities. However, if we expand I in a Taylor series about λ,

$$I(g, T, \mu, \lambda) = I(g, T, \mu, \lambda_{\text{obs}}) + \left.\frac{\partial I(g, T, \mu, \lambda)}{\partial \lambda}\right|_{\lambda_{\text{obs}}} (\lambda - \lambda_{\text{obs}}), \qquad (A2)$$

do the same for $\partial I/\partial T$, and use equation (7), our expression for the time-dependent flux becomes

$$F(\lambda_{\text{obs}}, t) = 2\pi R_0^2 \int_0^1 I(\mu, \lambda_{\text{obs}}) \mu \, d\mu$$

$$- R_0^2 \frac{\lambda_{\text{obs}}}{c} \int_0^1 \int_0^{2\pi} v_{\text{rad}} \, d\phi \left.\frac{\partial I(\mu, \lambda)}{\partial \lambda}\right|_{\lambda_{\text{obs}}} \mu \, d\mu$$

$$+ R_0^2 a_T \, e^{i\sigma t} \, e^{-i\psi} \int_0^1 \int_0^{2\pi} Y_{\ell m} \, d\phi \left.\frac{\partial I(\mu, \lambda_{\text{obs}})}{\partial T}\right|_{T_0} \mu \, d\mu. \qquad (A3)$$

We have suppressed the g and T dependences, which vanish upon choosing an equilibrium model. We have also left out the cross-term which includes the product of $\partial I/\partial T$ and $\partial I/\partial \lambda$ because these are both small quantities. The remaining expression contains separate terms for the equilibrium flux (F_0), the flux changes resulting from velocity shifts (ΔF_v), and the flux changes arising from temperature changes (ΔF_T). Using equation (A1), we can transform both v_{rad} and $Y_{\ell m}$ in the above integral into the coordinate system (θ, ϕ); for both, the terms with $m' \neq 0$ integrate to zero in the ϕ-direction (Dziembowski 1977), so only the $m = 0$ term aligned to our line of sight remains. Thus we may write

$$F(\lambda_{\text{obs}}, t) = F_0(\lambda_{\text{obs}}) + R^{\ell}_{0m} \Delta F_v(\lambda_{\text{obs}}, t, i = 0, m = 0)$$

$$+ R^{\ell}_{0m} \Delta F_T(\lambda_{\text{obs}}, t, i = 0, m = 0). \qquad (A4)$$

This expression permits us to relate $\Delta F/F(\lambda_{\text{obs}}, i \neq 0, m \neq 0)$ to $\Delta F/F(\lambda_{\text{obs}}, i = 0, m = 0)$ via a simple scaling factor R^{ℓ}_{0m}. As R^{ℓ}_{0m} does not depend on λ_{obs}, the results shown in Fig. 3 are general for arbitrary inclination and m value. Also, because the factor is the same for both the temperature- and velocity-induced flux changes, the observed ratio a_v/a_T does not depend on i and m. Finally, equation (A4) shows that the line-of-sight velocities and flux variations are separable to first order, a result used implicitly in Paper I.

It is important to recognize where these approximations may break down. When the second derivative of the spectrum dominates the first, which can happen in the central few ångstroms of an absorption line, our expansion to first order in λ is not reliable.

This paper has been typeset from a TEX/LATEX file prepared by the author.